Frontiers in Heat and Mass Transfer

Tech Science Press

Doi:10.32604/fhmt.2025.075848

ARTICLE

Multi-Objective Optimization of a Tapered Cathode Flow Channel in a Proton Exchange Membrane Fuel Cell

Wei Dong[1], Baoqi Guo[2], Weiwei Zhao[2], Hui Jian[2] and Zhenzong He[2,*]

[1]COMAC Beijing Aircraft Technology Research Institute, Beijing, 102211, China
[2]College of Energy and Power Engineering, Nanjing University of Aeronautics and Astronautics, Nanjing, 210016, China
*Corresponding Author: Zhenzong He. Email: hezhenzong@nuaa.edu.cn

Received: 10 November 2025; Accepted: 16 December 2025; Published: 30 April 2026

ABSTRACT: This study explores the design of a tapered cathode flow channel in a proton exchange membrane fuel cell (PEMFC), leveraging artificial intelligence and multi-objective optimization techniques to attain an optimal configuration. First, the influence of the channel height ratio and mass flow rate on PEMFC performance was systematically examined. The results reveal that decreasing the height ratio and increasing the mass flow rate lead to reduction in the standard deviation of current density, accompanied by a monotonic rise in pressure drop. The average current density initially rises before exhibiting a slight decline. Subsequently, a surrogate model based on a Backpropagation (BP) neural network was constructed, with height ratio and mass flow rate as input variables, to accurately predict the average current density, its standard deviation, and the channel pressure drop. The findings demonstrate that the BP-based surrogate model can reliably predict current density, its standard deviation, and channel pressure drop. The Mean Relative Errors (MREs) for current density, standard deviation, and pressure drop are 0.84%, 1.44%, and 1.77%, respectively, with all coefficients of determination (R^2) exceeding 0.999. Finally, Pareto optimal solutions for current density, standard deviation, and pressure drop of the tapered PEMFC were obtained through integration a multi-objective genetic algorithm. Results show that the optimized tapered PEMFC achieves the current density of 3141.41 A/m^2, the standard deviation of 53.58 A/m^2, and the channel pressure drop of 5.49 Pa. Compared with the conventional channel, the optimized PEMFC exhibits an 7.02% increase in current density and an 3.7% reduction in standard deviation, while maintaining the pressure drop within an acceptable range.

KEYWORDS: PEMFC; tapered flow channel; current density; multi-objective optimization

1 Introduction

The proton exchange membrane fuel cell (PEMFC) offers notable advantages, including low operating temperature, high power density, rapid start-up, robust stability, and environmental sustainability [1]. Consequently, it has been widely adopted in fields such as aerospace, military systems, power generation, electric vehicles, and portable power systems [2].

The flow channel is a critical component of the PEMFC, facilitating reactant transport and product removal, and directly influencing the fuel cell's overall performance and efficiency. It remains a key area of research in fuel cell technology [3]. Over recent decades, some researches [4,5] have shown that the design of optimized flow channel structures significantly enhances fuel cell performance, as well as the life cycle characteristics of the PEMFC [6]. Mohammedi et al. [2] examined the performance variations of PEMFCs featuring 30 distinct cross-sectional shapes for both the anode and cathode channels, all having identical

cross-sectional areas. The results revealed that the cross-sectional shape has a significant impact on PEMFC performance at high current density, with trapezoidal and semi-elliptical base shapes yielding superior power. Incorporating baffles represents another widely employed method to enhance PEMFC performance. Sun et al. [7] developed nine distinct types of baffles with varying cross-sectional shapes along the flow direction, which were applied to both sides of the PEMFC. Their study demonstrated that the combination of inverted trapezoids and rectangles exhibited the highest current density among nine configurations. While baffles can effectively enhance reactant supply to the catalyst layer, thereby improving PEMFC performance, they also induce an increase in pressure drop within the channel [8], resulting in higher power demand for the system's pump or compressor. To address this issue, researchers have recently proposed novel flow field designs inspired by biological systems and design principles to further improve reactant distribution and mass transfer efficiency. For example, Tan et al. [9] based on constructal theory and Murray's law, proposed an innovative flow field design. Their studies demonstrated that this novel flow field design provides a more balanced performance in terms of output power and overall pressure drop. Furthermore, strategies were proposed to enhance the uniformity of current density distribution in PEMFCs utilizing this design. Despite these promising performance enhancements, the complexity of its manufacturing process presents a significant barrier to large-scale application and commercialization.

The research predominantly focuses on fuel cells with constant-height channels. In fact, channels with gradually decreasing height along the gas flow—commonly referred to as tapered channels—represent an effective design strategy for enhancing fuel cell performance, with relatively straightforward fabrication processes. In traditional constant-height channels, the concentration of reactant gas progressively decreases along the flow direction due to its consumption. In contrast, in a tapered channel, the reduction in channel height (and corresponding decrease in cross-sectional area) helps to maintain, or even increase, the gas velocity in the downstream region, thereby enhancing the convective transport of gases to the porous electrode and increasing the cell's current density. Simultaneously, a higher concentration of reactants in the downstream region results in more uniform chemical reactions. The manufacturing process of the flow field plate is relatively straightforward as well. Although Wang et al. [10] proposed an effective flow field design, they did not account for the pressure changes induced by the tapered channel. Liu et al. [11] demonstrated that while tapered channels improve cell performance, they also introduce pressure losses. However, overall, the pressure losses are relatively low, and the practical potential of tapered channels has been validated. Neither Wang's nor Liu's research extensively investigated the structural parameters of tapered channel, lacking comprehensive investigation.

In fact, with the advancement of machine learning, an increasing number of studies employ ML techniques to construct intelligent and rapid prediction models for fuel cell channel performance, which are subsequently integrated with optimization techniques to achieve the optimal channel structure design. Xu et al. [12] optimized a system to maximum power density using neural networks and genetic algorithms. The results demonstrated that ANNs can effectively predict cell performance, and the optimized cell exhibited improved gas concentration distribution. Chen et al. [13] combined Response Surface Methodology (RSM) with the Non-dominated Sorting Genetic Algorithm (NSGA) to optimize fuel cell performance, targeting power density, system efficiency, and exergy efficiency as objective functions. The Pareto optimal solutions resulted in improvements of 13.18%, 7.06%, and 20.29% in power density, system efficiency, and exergy efficiency, respectively, compared to the straight channel. In summary, intelligent prediction models can rapidly and accurately assess fuel cell performance and can be integrated with optimization algorithms to identify global optimal solutions.

These findings demonstrate the substantial influence of flow channel geometry on fuel cell performance and the unique benefits of tapered configurations. Nevertheless, prior work has been narrowly focused on

analyzing individual, predefined tapered designs. A significant gap persists in the literature regarding the systematic multi-objective optimization of such channels to enhance current density and reduce pressure drop simultaneously. This study considers a simplified channel structure and integrates computational fluid dynamics (CFD) modeling with neural networks and genetic algorithms to optimize the design of the PEMFC with tapered channel, thereby achieving performance optimization. Firstly, a 3D single-channel simulation model was developed to investigate the effects of the tapered channel height ratio and mass flow rate on the PEMFC performance, and the changing of the current density and pressure drop were obtained. Moreover, a database correlating the tapered channel height ratio and mass flow rate with the current density and pressure drop were established. Based on this, a high-precision surrogate model was established using a BP neural network to predict the average current density, standard deviation, and channel pressure drop. Finally, multi-objective optimization technology was performed using the nondominated sorting genetic algorithm II (NSGA II) and the Linear Programming Technique for Multidimensional Analysis of Preference (LINMAP) to obtain the optimal channel height ratio and the corresponding cell performance.

2 CFD Model

2.1 Geometric Model

Fuel cells with conventional channel and tapered channel are schematically shown in Fig. 1. The basic geometric parameters are listed in Table 1. The inlet geometric parameters of the PEMFC with conventional channel and tapered channel are identical, while the outlet geometric parameters remain unchanged. The ratio of the outlet cross-sectional height to the inlet cross-sectional height for the tapered flow channel is defined as $\pi = H_{out}/H_{in}$. The PEMFC primarily consists of seven parts: the anode and cathode gas channels, the anode and cathode gas diffusion electrodes (GDEs), the anode and cathode catalyst layers (CLs), and the proton exchange membrane. H_2 enters the anode, passes through the gas diffusion layer to reach the catalyst layer, where catalyzed by the anode catalyst, a hydrogen molecule is oxidized into two protons (H^+), releasing two electrons. Protons are transported through the electrolyte membrane to the cathode via hydration, while electrons travel through the diffusion layer and bipolar plate to the external circuit, eventually reaching the cathode catalyst layer. Oxygen or air enters the cathode, passing through the cathode diffusion layer, undergoes a reduction reaction at the cathode catalyst layer, reacting with protons and electrons to form H_2O (liquid or vapor). Compared to the anode, the slower cathode reaction is the main factor limiting PEMFC performance [14]. Therefore, the cathode side of a high-temperature PEMFC is selected as the research subject in the paper. Moreover, this paper focuses on high-temperature proton exchange membrane fuel cells (HT-PEMFCs), which operate at a working temperature of 373 K. It is assumed that the generated water remains in a gaseous state throughout the process, and the issue of water phase change does not arise.

2.2 Conservation Equations

The mass, heat, and charge transport processes within the PEMFC are governed by the following conservation equations: mass conservation, momentum conservation, species conservation, energy conservation, liquid water and dissolved water conservation, and proton and electron transport equations, as detailed in Refs. [15–17].

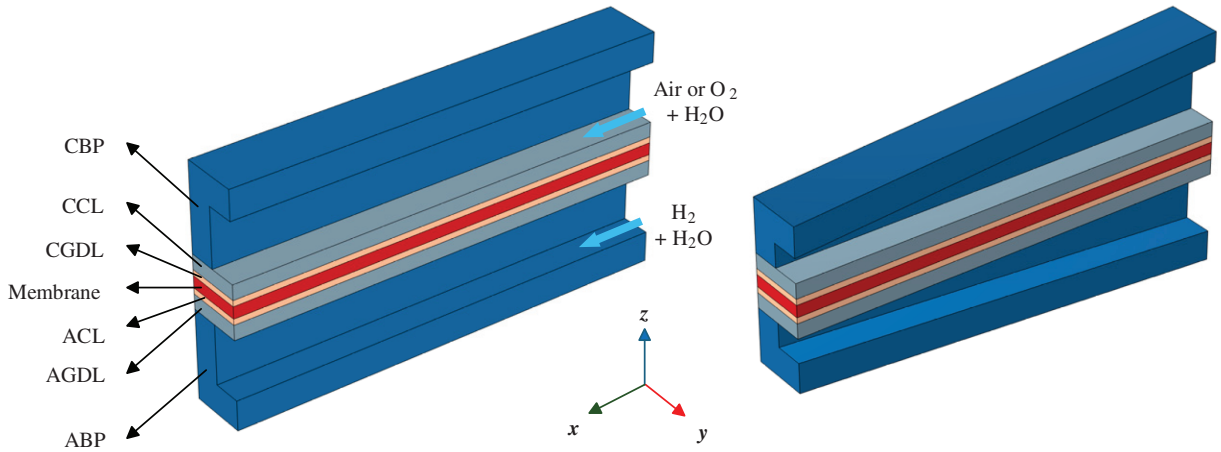

Figure 1: Schematics of a PEMFC with conventional channel (**left**), tapered channel (**right**)

Table 1: The geometric parameters of the PEMFC

Parameters	Value
Channel length L	22.36 mm
Channel width W_{ch}	1.8 mm
Rib width W_{rib}	1.8 mm
Thickness of GDL H_{gdl}	0.2 mm
Channel inlet height H_{in}	1.8 mm
Channel outlet height H_{out}	–
Height ratio of channel inlet and outlet π = Hout/Hin	–

Mass conservation equation:

$$\nabla \cdot \left(\varepsilon \rho \vec{u}\right) = S_m \tag{1}$$

where ρ is gas density, $\vec{u}$ is gas velocity, and S_m is the mass source term.

Momentum conservation equation:

$$\nabla \cdot \left(\varepsilon \rho \vec{u}\vec{u}\right) = -\varepsilon \nabla p + \nabla \cdot \left(\varepsilon \mu \nabla \vec{u}\right) + S_{mom} \tag{2}$$

where ε is porosity, p is pressure, μ is gas dynamic viscosity, and S_{mom} is the momentum source term.

Energy conservation equation:

$$\nabla \cdot \left(\varepsilon \rho c_p \vec{u} T\right) = \nabla \cdot \left(k_{eff} \nabla T\right) + S_E \tag{3}$$

where c_p is specific heat capacity, T is temperature, k_{eff} is effective thermal conductivity, and S_E is the energy source term.

Species transport equation:

$$\nabla \cdot \left(\vec{u} \varepsilon c_i\right) = \nabla \cdot \left(D_i^{eff} \nabla c_i\right) + S_i \tag{4}$$

where c_i is species volume fraction, D_i^{eff} is effective species diffusion coefficient, and S_i is the species source term.

Charge conservation equation:

$$\nabla \cdot (\sigma_{sol,mem} \nabla \varphi_{sol,mem}) + \overline{R}_{sol,mem} = 0 \tag{5}$$

where the subscripts sol and mem represent the solid phase and membrane phase, respectively; σ, φ and $\overline{R}$ represent conductivity, potential, and volumetric transfer current, respectively.

Water saturation equation:

$$\nabla \cdot \left[\rho_l \frac{K_{s^\gamma}}{\mu_l} \frac{dp_c}{ds} \nabla \cdot s \right] = r_w \tag{6}$$

where s is water saturation, r_w is condensation rate, and P_c is capillary pressure. Table 2 shows the Source terms for governing equations in the model.

Table 2: Source terms for governing equations in the model [15–17]

Conservation equation	Source terms
Mass	CL: $S_m = -\frac{M_{O_2}}{4F} R_{cat} + \frac{M_{H_2O}}{2F} R_{cat} + \frac{n_d M H_2O}{F} R_{cat}$ Other domains: $S_m = 0$
Momentum	$S_{mom} = 0$
Energy	Bipolar plate: $S_E = \frac{I^2}{\sigma_s}$ GDL: $S_E = \frac{I^2}{\sigma_s^{eff}} + h_L r_W$ CL: $S_E = R_{an,cat}\eta_{an,cat} + \frac{I^2}{\sigma_s^{eff}} + \frac{I^2}{\sigma_m^{eff}} + h_L r_W$
Species	MEM: $S_E = \frac{I^2}{\sigma_m^{eff}}$ CL: $S_{O_2} = -\frac{M_{O_2}}{4F} R_{cat}$ $S_{H_2O} = \frac{M_{H_2O}}{2F} R_{cat} + \frac{n_d M H_2O}{F} R_{cat} - r_W$

The local current density is defined by the Butler-Volmer equation:

$$i_{loc} = i_0 \frac{C_{O_2}}{C_{O_{2_{ref}}}} \left(\exp\left(\frac{\alpha_c}{R_g T} F \eta_c \right) - \exp\left(-\frac{1-\alpha_c}{R_g T} F \eta_c \right) \right) \tag{7}$$

where i_0 represents the exchange current density, C_{O_2} and $C_{O_{2_{ref}}}$ represent the oxygen molar concentration and reference oxygen molar concentration, respectively. η_c represents the cathode overpotential.

The cathode overpotential is calculated as follows:

$$\eta_c = E_{Nernst} - V_{cell} - R_0 i_{loc} \tag{8}$$

where E_{Nernst} is the Nernst potential, R_0 is the resistance, and V_{cell} is the actual operating voltage. The Nernst potential is calculated as follows:

$$E_{Nernst} = 1.229 - 0.87 \times 10^{-3} \left(T - 298.15\right) + \frac{RT}{2F}\left[\ln p_{H_2} + \frac{1}{2}\ln p_{O_2}\right] \tag{9}$$

where p_{H_2} and p_{O_2} are the partial pressures of hydrogen and oxygen, respectively, R is the universal gas constant, and F is the Faraday constant.

The average current density of the fuel cell $\bar{i}_{loc}$, and the standard deviation of the current density distribution, $\theta_{i_{loc}}$, are described as follows:

$$\bar{i}_{loc} = \frac{\int i_{loc} ds}{\int ds} \tag{10}$$

$$\theta_{i_{loc}} = \sqrt{\frac{\int \left(i_{loc} - \bar{i}_{loc}\right)^2 ds}{\int ds}} \tag{11}$$

2.3 Boundary Conditions

The model operating conditions and inlet parameters are shown in Table 3. Mass flow rate is used at the inlet, and the gas outlet is set to a pressure boundary condition, fixed at 1 atm. The channel walls are no-slip boundaries, while slip boundary conditions are considered at the electrodes. Moreover, the mass fractions of oxygen, water, and nitrogen being 0.228, 0.023, and 0.749, respectively. The outlet condition is atmospheric pressure, and the manifold effect is not considered. Thermal convection occurs on the wall surfaces of the flow channels, while the influence of thermal radiation is neglected.

Table 3: Model operating conditions and inlet parameters

Parameters	Value
Stoichiometric coefficient of H_2O, υ_{H_2O}	2
Stoichiometric coefficient of N_2, υ_{N_2}	0
Stoichiometric coefficient of O_2, υ_{O_2}	−1
Operating voltage, V_{cell}	0.4 V
Ohmic resistance, R_0	7e−5 Ω·m^2
Cathodic transfer coefficient, α_c	0.5
Oxygen inlet mass fraction, $w_{O_2,\text{in}}$	0.228
Water inlet mass fraction, $w_{H_2O,\text{in}}$	0.023
Nitrogen inlet mass fraction, $w_{N_2,\text{in}}$	0.749
Inlet mass flow rate, m	kg/s
Operating temperature, T	373 K
Operating pressure, P	101,325 Pa
Porosity of the GDL, ε	0.8
Permeability of the GDL, κ_{GDL}	1.38e−11 m^2
Dynamic viscosity, μ	2.07e−5 Pa·s
Exchange current density, i_0	0.17 A/m^2

2.4 Grid Independence Verification and Model Validation

The computational grid for the PEMFC model with tapered channel is shown in Fig. 2. A structured grid was used. Since the diffusion layer is thin, the grid was refined at the interface between the diffusion layer and the channel to improve computational accuracy. Besides, when the PEMFC operating voltage is 0.4 V, the relative errors of current density between grid systems with 1120, 22,400 and 51,200 elements are limited within 3%. Therefore, the grid system with 22,400 elements is dense enough and adopted in subsequent study to save computational resources and time while ensuring result accuracy.

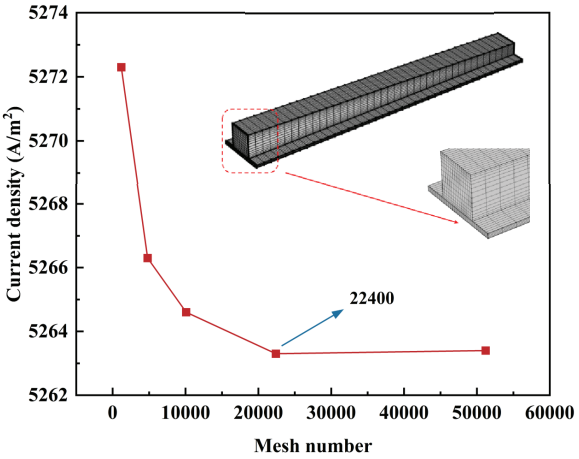

Figure 2: The result of the grid independence testing

To ensure the reliability of the numerical model, the model geometry, operating conditions, and other key parameters were kept consistent with the experiment of Haghayagh et al. [18]. The polarization curve obtained from the numerical simulation in this study and the experimental data from Haghayagh is shown in Fig. 3. From Fig. 3, it can be observed that the simulation results closely match the experimental data, with a maximum error not exceeding 6%. Therefore, the model is suitable for simulating the performance of PEMFC.

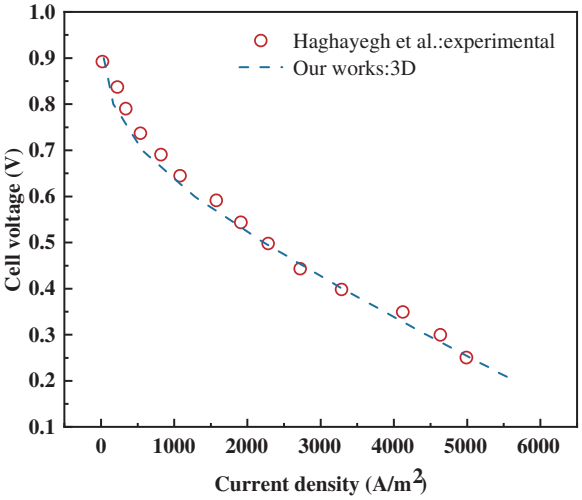

Figure 3: Model validation: comparison of polarization curve between simulation and experiment [18]

3 Results and Discussion

3.1 Effect of Mass Flow Rate and Height Ratio on PEMFC Performance

This section investigates the effects of varying mass flow rates and height ratios (as defined in Table 1) on the performance of the PEMFC with a tapered channel, including current density, standard deviation, and channel pressure drop. In this study, the values of height ratio of channel inlet and outlet π were set to 0.1, 0.2, 0.3, 0.4, 0.5, 0.6, 0.7, 0.8, 0.9, and 1.0, while maintaining a constant channel inlet height. The values of inlet mass flow rate m were set to 2.5e−7, 5.0e−7, 7.5e−7, 1.0e−6, and 1.25e−6 kg/s, respectively. The description of cases is provided in Table 4, labeled A~E for increasing values of m, and 1~10 for increasing values of π. Unless otherwise specified, the cell operating voltage in this paper is 0.4 V.

Table 4: Description of the simulated cases regarding the various π and m

H_{in} (mm)	H_{out} (mm)	π	Inlet mass flow rate, m ($\times 10^{-7}$ kg/s)				
			2.5	**5.0**	**7.5**	**10.0**	**12.5**
1.8	0.18	0.1	A1	B1	C1	D1	E1
	0.36	0.2	A2	B2	C2	D2	E2
	0.54	0.3	A3	B3	C3	D3	E3
	0.72	0.4	A4	B4	C4	D4	E4
	0.9	0.5	A5	B5	C5	D5	E5
	1.08	0.6	A6	B6	C6	D6	E6
	1.26	0.7	A7	B7	C7	D7	E7
	1.44	0.8	A8	B8	C8	D8	E8
	1.62	0.9	A9	B9	C9	D9	E9
	1.8	1.0	A10	B10	C10	D10	E10

3.1.1 Effect on Current Density

Fig. 4 depicts the effect of m and π on the current density of the PEMFC with tapered channel. It can be seen that for a constant height ratio, as the channel mass flow rate increases, the current density of the fuel cell exhibits an increasing trend, with the rate of increase gradually slowing as the mass flow rate rises. This phenomenon can be explained from Fig. 5. Fig. 5 presents the distribution of current density in the catalyst layer at different mass flow rates when the π = 0.9. It is evident that as the mass flow rate increases, the current density increases, and the current distribution within the latter part of the cell becomes more uniform. This behavior is attributed to the fact that the electrochemical reaction in the PEMFC is reliant on an adequate supply of reactants. As the inlet mass flow rate increases, the oxygen partial pressure at the cathode also increases. According to the Nernst equation (Eq. (9)), higher gas partial pressure boosts the cell's open-circuit voltage, thus enhancing the driving force of the reaction, accelerating the reaction rate, and consequently increasing current density. Additionally, increasing the mass flow rate enhances oxygen transport efficiency, reduces the concentration gradient in the diffusion layer, and minimizes concentration polarization, which further contributes to the increase in the cell's current density. Since the diffusion coefficient of anode hydrogen is typically large and the associated limitations are minimal, this study considers only the cathode half-model. In fact, the anode hydrogen transport process is analogous, and adequate gas supply also facilitates the maintenance of a high reaction rate.

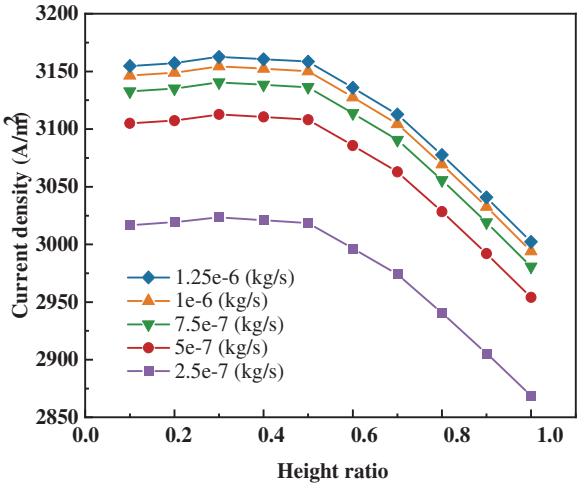

Figure 4: Performance of PEMFC under different m and π

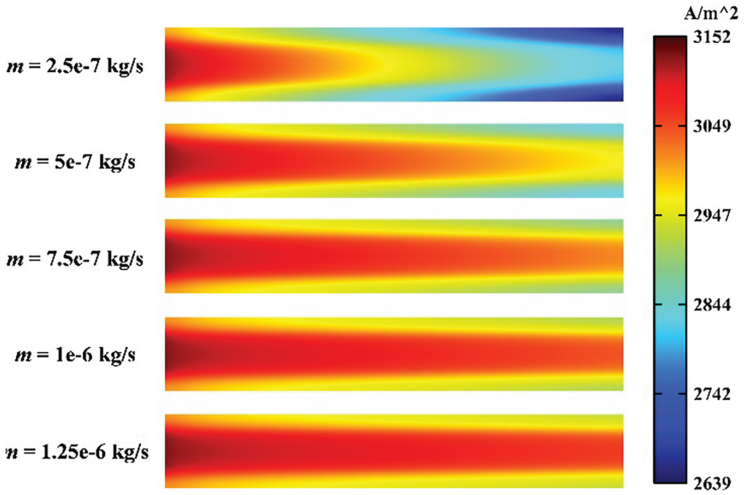

Figure 5: Current density distribution under different *m*

As observed in Fig. 4, for a constant mass flow rate, a decrease in π initially causes a significant increase in current density, followed by a slight decline, with the maximum value occurring near $\pi = 0.3$. This behavior suggests the existence of an optimal fuel cell channel height ratio, where current density is maximized. The explanation for the behavior can be seen from Fig. 6. Fig. 6 depicts the current density distribution in the catalyst layer for different values of π at a mass flow rate of 7.5e−7 kg/s. Results reveal that as the channel height ratio decreases, the current density generally increases. This behavior is due to the fact that the reactant gas concentration is highest at the channel inlet, leading to the highest current density. As the gas flows along the channel, the gas concentration progressively decreases, eventually becoming insufficient to maintain an adequate concentration gradient for the reaction. The reduction in channel height increases the gas volumetric density in the channel, facilitating the ingress of gas into the catalyst layer for the reaction, thereby enhancing the current density.

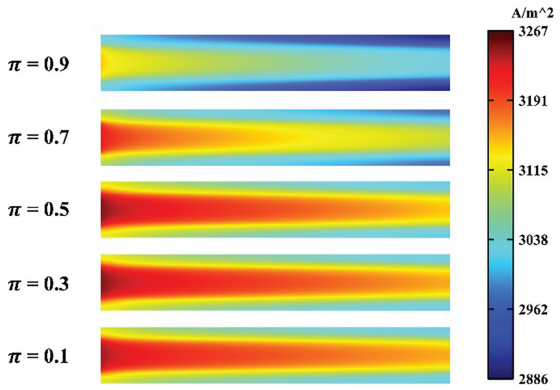

Figure 6: Current density distribution under different π

Furthermore, the mechanism underlying the height ratio's effect on current density can also be seen from the oxygen molar concentration distribution at various cross-sections along the channel direction, as show in Fig. 7. In Fig. 7, m is set to 7.5e−7 kg/s, with height ratios of 0.1, 0.3, 0.5, 0.7, and 0.9, respectively. The cross-sections S1, S2, S3, and S4 are situated at 1/5, 2/5, 3/5, and 4/5 of the channel length, measured from the inlet. It can be seen that as the π decreases, the oxygen concentration in the channel decreases, indicating that more gas enters the diffusion layer to participate in the electrochemical reaction. This is because the reduction in channel height ratio decreases the channel cross-sectional area. According to mass conservation, the gas velocity increases. Higher velocity helps increase the reactant gas concentration gradient and improve cell voltage. However, as the height ratio continues to decrease, the rate of current density increase gradually diminishes, and a slight decrease is observed once the height ratio reaches 0.3. This occurs because reducing the height ratio below 0.3 significantly increases gas velocity, leaving insufficient residence time in the reaction layer before expulsion. Consequently, diminished oxygen diffusion reduces the supply to the catalyst layer, slowing the electrochemical reaction rate and lowering current density. This trend, where further reductions in channel height yield diminishing returns, aligns with the law of diminishing marginal returns.

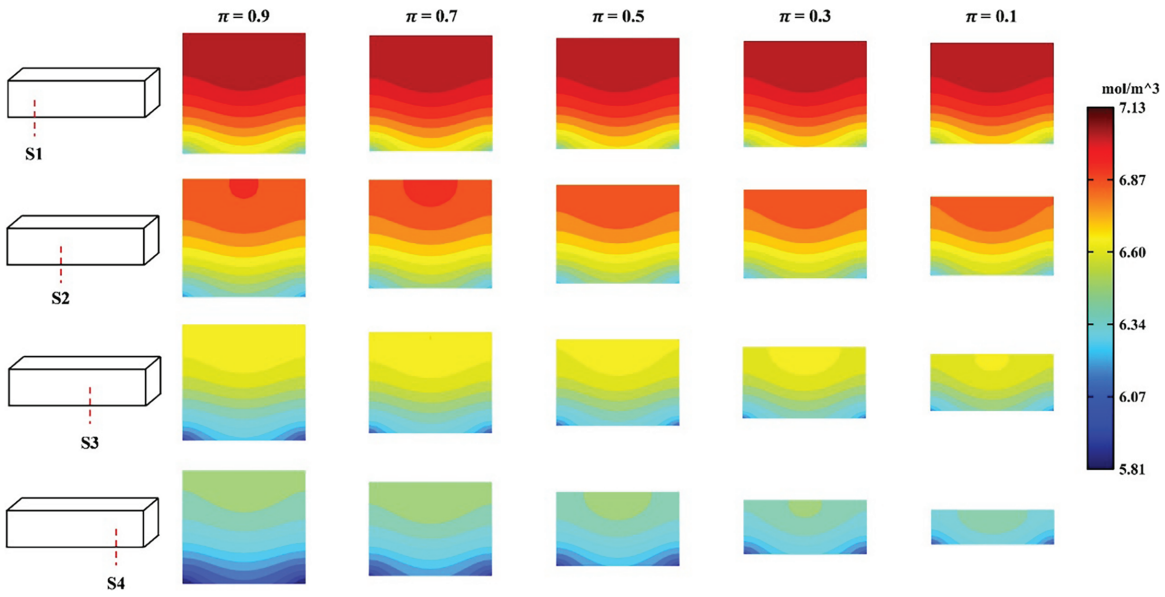

Figure 7: Oxygen molar concentration distribution under different π

3.1.2 Effect on Standard Deviation

Fig. 8 illustrates the variation of the standard deviation of current density for the PEMFC with tapered channel under different m and π. It can be seen that as π decreases, the standard deviation shows a decreasing trend; as m increases, the standard deviation similarly decreases. Specifically, when m increases from 2.5e−7 kg/s to 7.5e−7 kg/s, the standard deviation decreases significantly, indicating a substantial improvement in current density uniformity. However, when m increases further beyond 7.5e−7 kg/s, the decrease in standard deviation becomes slower, suggesting diminishing returns for further improvement in uniformity. This indicates that increasing the mass flow rate can effectively improve current density uniformity, but it is also apparent that the improvement diminishes as the mass flow rate continues to increase. This can be attributed to the fact that an increase in inlet mass flow rate raises the reactant gas velocity, thereby shortening the gas residence time within the channel. As a result, some gas is expelled before fully participating in the electrochemical reaction, leading to lower reactant utilization. Given that the reactant gas fed into the channel is air, if the mass flow rate is excessively high, oxygen may not have enough time to fully diffuse into the catalyst layer. This results in localized oxygen starvation and performance degradation, negatively impacting the uniformity of the electrochemical reaction and yielding minimal benefits for current density uniformity.

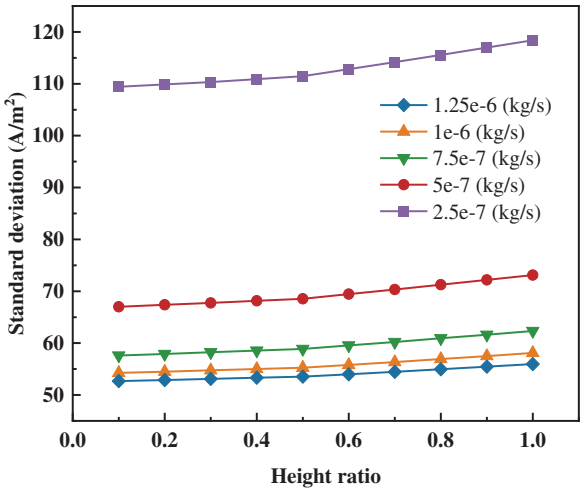

Figure 8: Standard deviation of current density under different m and π

3.1.3 Effect on Pressure Drop

Fig. 9 illustrates the variation of the pressure drop for the PEMFC with tapered channel under different m and π. It can be seen that although increasing the inlet mass flow rate boosts the current density, it also results in a rise in pressure drop within the channel, leading to additional power consumption. Taking the mass flow rate of 7.5e−7 kg/s as an example, it can be found that when the height ratio decreases from 1.0 to 0.5, the pressure drop gradually increases. This is because the channel cross-section decreases, increasing the flow resistance. As the height ratio decreases from 0.5 to 0.3, the rate of increase in pressure drop slightly accelerates, though it remains within a reasonable range. When the height ratio decreases from 0.3 to 0.1, the pressure drop increases sharply. This phenomenon can be explained by analogy to Darcy's law and the Poiseuille law, which state that pressure loss in microchannels exhibits a nonlinear relationship with channel size/height, as expressed in the following equation [19]:

$$\Delta p \propto \frac{1}{D^4} \tag{12}$$

where D represents the equivalent diameter of the channel. Therefore, when the height ratio is too small, the equivalent diameter decreases, causing a significant increase in the inlet-outlet pressure difference. This phenomenon is highly unfavorable for reducing pump power consumption. Therefore, height ratios below 0.3 are not considered.

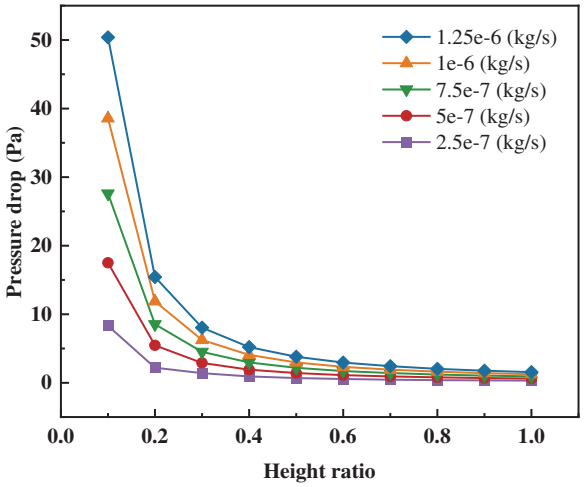

Figure 9: Pressure drop under different m and π

In summary, variations in the height ratio can affect gas transport, current density uniformity and pressure drop in the PEMFC with tapered channel. However, overall, the decreasing in the height ratio of inlet and outlet has a consistent effect on improving both current density and its uniformity.

3.2 Construction of a High-Precision Surrogate Model

This section aims to develop a high-precision prediction model for the average current density, current density standard deviation, and pressure drop of the PEMFC, which is a multi-input multi-output problem. The BP neural network is a multi-layer feedforward network with high self-learning and adaptive capabilities. It typically consists of an input layer, hidden layers, and an output layer. The feedforward network sequentially transmits information from the input layer to the hidden layers and subsequently to the output layer. Different layers are interconnected via neurons, where each neuron structure is used for information reception and transmission and can be regarded as a specific output function—the activation function (AF). A commonly used activation function is defined as follows:

$$f(x) = 1/(1 + e^{-x}) \tag{13}$$

Based on the 50 cases from Section 3.1, the height ratio and mass flow rate are selected as input parameters, and average current density, standard deviation, and channel pressure drop of the PEMFC are selected as output parameters. Therefore, the number of neurons in the input and output layers is 2 and 3, respectively. The number of neurons in the hidden layer is determined using the following empirical formula:

$$i' = 2s' + 1 \text{ or } i' = \sqrt{s' + t} + a \tag{14}$$

where i' is the number of input neurons, s' is the number of hidden neurons, t is the number of output neurons, and a is an integer between [0, 10].

The 50 datasets obtained in Section 3.1 are randomly divided for training, testing, and validation sets, accounting for 80%, 10%, and 10%, respectively. The validation set is utilized to prevent model overfitting. The topology of the BP neural network is illustrated in Fig. 10.

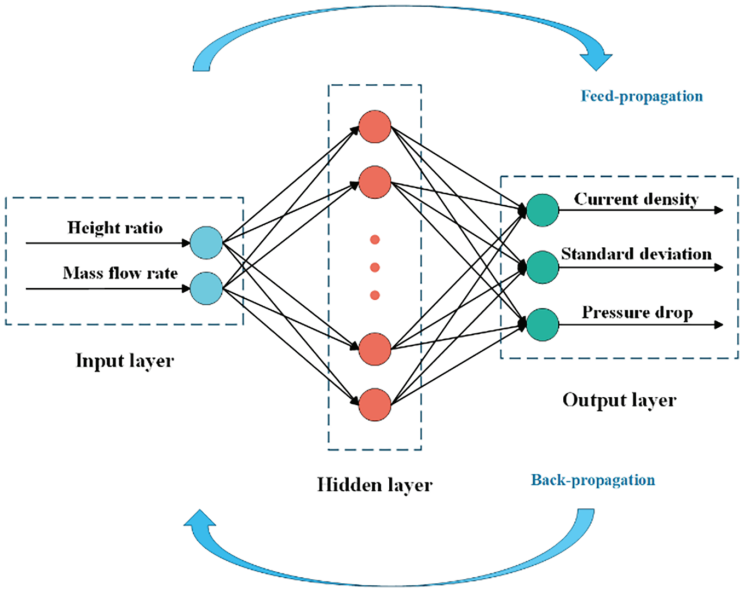

Figure 10: Topology of BP neural network

The accuracy of the neural network is evaluated using the Mean Relative Error (MRE) and the Coefficient of Determination (R^2), defined as follows:

$$MRE = \frac{1}{N}\sum_{i=1}^{N}\left|\frac{y_i - y_i^-}{y_i}\right| \times 100\% \tag{15}$$

$$R^2 = 1 - \frac{\sum_{i=1}^{n}(y_i - y_i^-)^2}{\sum_{i=1}^{n}(\overline{y} - y_i)^2} \tag{16}$$

where N represents the number of test samples, y_i represents the true value, y_i^- represents the model predicted value, and $\overline{y}$ represents the average of the true values. MRE indicates the deviation between the true and predicted values, and R_2 is used to measure the degree to which the model's predicted output explains the actual value. In general, the closer the MRE is to 0 and the closer R^2 is to 1, the higher the reliability of the model.

The selection of the neural network architecture is mainly based on three factors: topology, training algorithm, and activation function. The topology primarily considers the number of hidden layers and neurons. Since there are 2 input variables and 3 output parameters, the input layer and output layer are designed with 2 and 3 neurons, respectively. The activation function enables the neural network to handle nonlinear problems and enhances its function approximation capability. Both the training algorithm and hyperparameters also exert an impact on the convergence and accuracy of the model. Referring to relevant studies and preliminary work, the hyperparameter settings of the BP neural network in this study are as follows: the number of hidden layer neurons is set to 12, which achieves a good balance between network complexity and generalization ability. The tansig function is adopted as the activation function, the number

of training epochs is set to 2000, and the learning rate is 0.001. Fig. 11 presents a comparison between the numerical simulation results and the predictions of the surrogate model. Based on the calculation, the MRE of current density, standard deviation, and pressure drop are 0.84%, 1.44%, and 1.77%, respectively. And R^2 are all above 0.999. Therefore, the prediction model proposed in this study is considered capable of providing design guidance for PEMFC performance optimization.

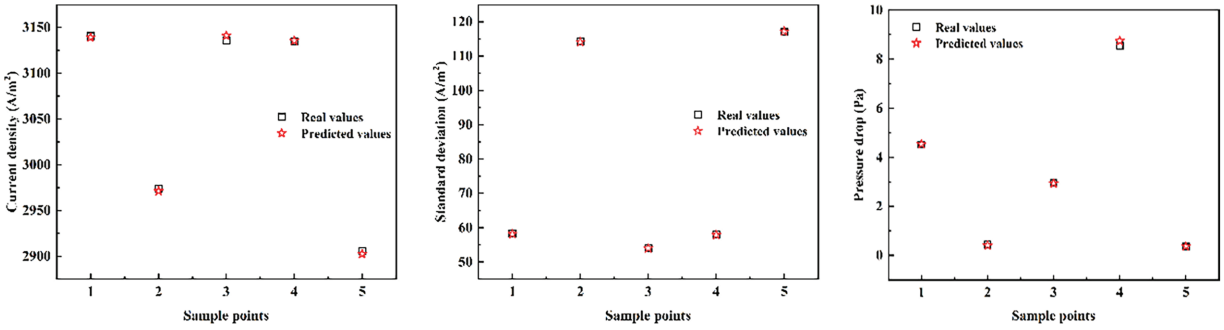

(a) Current density (b) Standard deviation (c) Pressure drop

Figure 11: Comparison between the surrogate model and CFD model: (**a**) current density; (**b**) standard deviation; (**c**) pressure drop

3.3 Multi-Objective Optimization Using NSGA-II

This section combines the BP neural network and NSGA-II to optimize the performance of PEMFC. Based on the well-trained neural network model, the genetic algorithm is employed to perform online optimization of the Pareto optimal solutions for the PEMFC current density, standard deviation, and pressure drop.

During the search process for various possible optimal designs of the PEMFC using the genetic algorithm, a large number of possible solutions are generated. The set of non-dominated solutions is referred to as the Pareto solution set. Since different weights can be assigned to each objective parameter under different scenarios, the genetic algorithm solving the comprehensive objective function can obtain a set of Pareto solutions and one optimal solution that minimizes the comprehensive objective function for each scenario. The objective functions in this study are maximum average current density, minimum standard deviation, and minimum channel pressure drop.

The Pareto solution set obtained in this study is presented in Fig. 12. To decide an optimal tapered channel solution among the three objectives, the LINMAP method is employed to perform a trade-off between current density, standard deviation and pressure drop. The LINMAP method identifies the optimal solution by calculating the Euclidean distance between the Pareto and ideal solutions [20]. The optimal tapered channel solution in this study (marked by a star in Fig. 12) is 3161.28 A/m^2 for current density, 53.31 A/m^2 for current density standard deviation, 5.65 Pa for pressure drop when π = 0.385, m = 12.46e−7 kg/s. The CFD simulation results for the optimal model (with a height ratio of 0.385) were also obtained using the input parameters corresponding to the Pareto optimal solution. As shown in Table 5, the CFD numerical simulation of the PEMFC at the optimal height ratio yielded the average current density of 3141.41 A/m^2, the standard deviation of 53.58 A/m^2, and the pressure drop of 5.49 Pa. Additionally, the CFD numerical simulation of the PEMFC at π = 1 (for the conventional channel) were also obtained, which yielded the average current density of 2935.31 A/m^2, the current density standard deviation of 55.63 A/m^2, and the pressure drop of 1.54 Pa. Fig. 13 illustrates the current density distribution of the PEMFC with conventional channel and optimal tapered channel at an operating voltage of 0.4 V. It can be seen that during the reaction,

the current density reaches its maximum at the channel inlet and gradually decreases along the gas flow direction. Compared with the conventional channel, although the pressure drop of the PEMFC with the optimal tapered channel increases, the magnitude of the increase is relatively small. Therefore, the increase in channel pressure drop due to height ratio reduction remains within a reasonable range. Compared to the results of the conventional channel, the current density increased by 7.02% and the current density standard deviation decreased by 3.7%, while the pressure drop increased 4.11 Pa. Therefore, the channel with the optimal height ratio can achieve higher current density and power density while enhancing the uniformity of the cell current distribution.

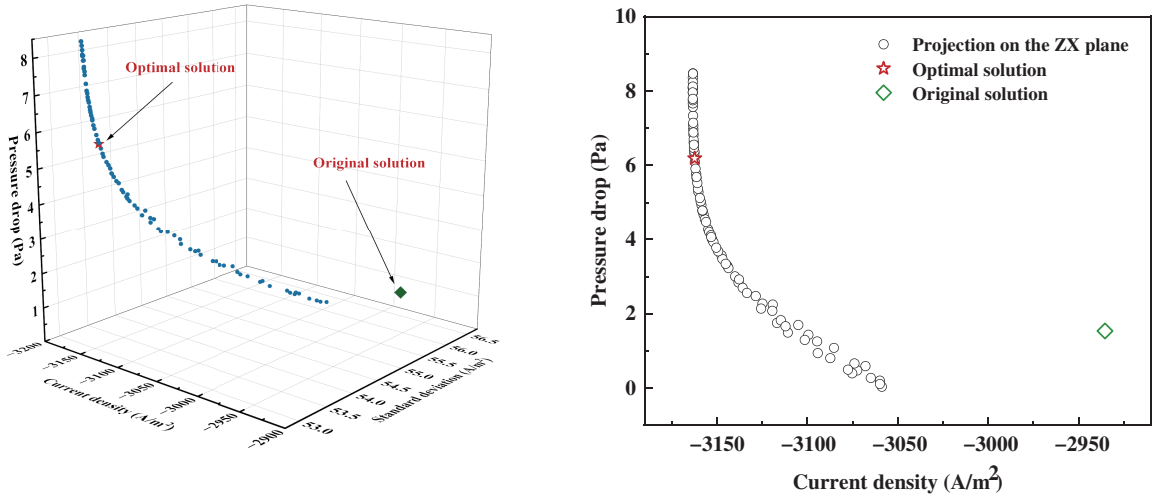

(a) Three-dimensional results

(b) Two-dimensional projection

Figure 12: Pareto frontier curve of the optimization results. (**a**) Three-dimensional results; (**b**) Two-dimensional projection

Table 5: Comparison of calculation results between conventional channel and optimal channel

	Current density (A/m^2)	Current density standard deviation (A/m^2)	Pressure drop (Pa)
CFD model: conventional channel	2935.31	55.63	1.54
Surrogate model: optimal channel	3161.28	53.31	5.65
CFD model: optimal channel	3141.41	53.58	5.49

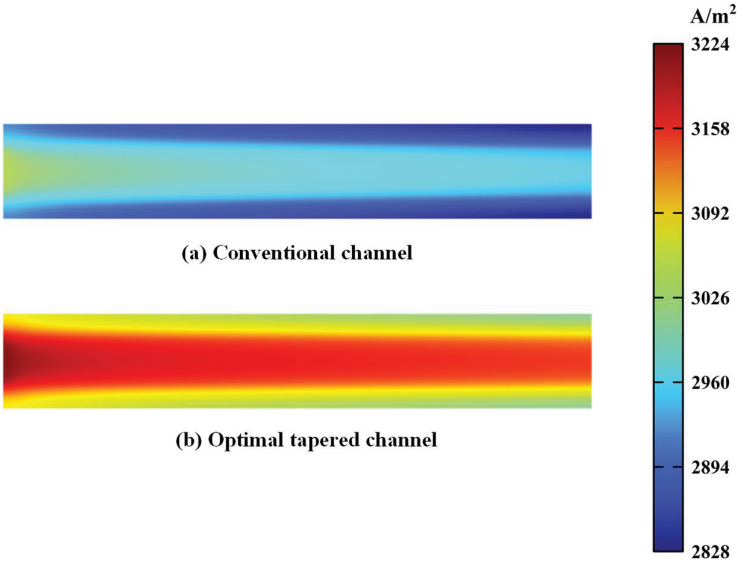

Figure 13: Current density distribution of PEMFC with conventional channel and tapered channel

4 Conclusion

This study focused on the PEMFC with tapered cathode channel, exploring the influence of the channel height ratio and mass flow rate on the performance of the PEMFC, and obtained an optimized tapered PEMFC channel configuration by combining artificial intelligence and multi-objective optimization techniques. The conclusions are as follows:

(1) The average current density exhibits a non-monotonic trend with decreasing height ratio, reaching its maximum near $\pi = 0.3$. This peak performance is associated with enhanced current density uniformity (lower standard deviation) at the cost of a higher channel pressure drop.

(2) Increasing the mass flow rate improves both the average current density and its uniformity while raising the pressure drop. The magnitude of these effects, however, decreases with further increments in flow rate.

(3) A surrogate model based on a BP neural network demonstrates excellent predictive capability for PEMFC performance. Its accuracy is validated by low mean relative errors (MRE < 1.8%) and near-unity R^2 values (>0.999) for all three output parameters.

(4) Compared with the conventional channel, the PEMFC with the optimally designed tapered channel configuration obtained through multi-objective optimization methods exhibits 7.02% increase in current density, 3.7% reduction in standard deviation, while maintaining the channel pressure drop an acceptable range. The fuel cell stack developed based on the variable-cross-section flow channel configuration proposed in this paper achieves higher current density and lower pressure drop. This will to a certain extent alleviate the issue of low power density associated with traditional fuel cell stacks, verifying that the proposed configuration is worthy of further experimental research and promotion.

Although an effective optimization design and methodology are proposed in this paper, there are still some limitations. First, to simplify calculations and save computational time, this study does not consider contact resistance, degradation mechanisms, and aging issues in detail; moreover, complex processes such as water transport and phase change are either simplified or neglected. Second, the model is based on a steady-state assumption, and thus cannot directly evaluate the transient response of the designed scheme. In addition, the research object of this paper is a single flow channel, failing to take into account factors such

as inter-channel interactions and uneven gas supply distribution, which may exert a significant impact on the performance of actual fuel cell stacks. Future research will focus on addressing these issues to further improve the accuracy and applicability of the model.

Acknowledgement: Not applicable.

Funding Statement: This project is supported by the Natural Science Foundation of Jiangsu Province (BK20231445); Aeronautical Science Foundation of China (20230028052001).

Author Contributions: All authors have contributed equally to this work. Wei Dong, Baoqi Guo, Weiwei Zhao, Hui Jian and Zhenzong He conceived the structure of paper; methodology, Wei Dong and Zhenzong He; investigation, Hui Jian and Baoqi Guo; writing—original draft preparation, Wei Dong and Weiwei Zhao. All authors reviewed the results and approved the final version of the manuscript.

Availability of Data and Materials: The authors confirm that the data used in this study is available on request.

Ethics Approval: Not applicable.

Conflicts of Interest: The authors declare no conflicts of interest to report regarding the present study.

Nomenclature

$\vec{u}$	Gas velocity
S_m	The mass source term
p	Pressure
S_{mom}	The momentum source term
T	Temperature
S_E	The energy source term
D_i^{eff}	Effective species diffusion coefficient
$\overline{R}$	Volumetric transfer current
r_w	Condensation rate
p_c	Capillary pressure
E_{Nernst}	The Nernst potential
R_0	The resistance
V_{cell}	The actual operating voltage
i_{loc}	The local current density
p_{H_2}	The partial pressures of hydrogen
p_{O_2}	The partial pressures of oxygen
R	The universal gas constant
F	The Faraday constant
$\bar{i}_{loc}$	The average current density of the fuel cell
D	The equivalent diameter of the channel
i'	The number of input neurons
s'	The number of hidden neurons
t	The number of output neurons
N	The number of test samples
y_i	Represents the true value
$\bar{y_i}$	Represents the model predicted value
$\overline{y}$	Represents the average of the true values
MRE	Indicates the deviation between the true and predicted values
R^2	Measure the degree to which the model's predicted output explains the actual value

i_0	The exchange current density
C_{O_2}	The oxygen molar concentration
$C_{O_{2_{ref}}}$	Reference oxygen molar concentration
c_p	Specific heat capacity
k_{eff}	Effective thermal conductivity
c_i	Species volume fraction
S_i	The species source term
s	Water saturation

Greek symbols

ρ	Gas density
ε	Porosity
μ	Gas dynamic viscosity
σ	Conductivity
φ	Potential
η_c	Represents the cathode overpotential
$\theta_{i_{loc}}$	The standard deviation of the current density distribution
a	An integer between [0, 10]
π	The ratio of the outlet cross-sectional height to the inlet cross-sectional height for the tapered flow channel

Subscripts

sol	Solid phase
mem	Membrane phase
eff	Refer to effective
cell	Refer to battery
Nerst	Refer to Nernst
loc	Refer to local
ref	Refer to reference
O_2	Refer to oxygen
H_2	Refer to hydrogen
mom	Refer to momentum

References

1. Duan F, Song F, Chen S, Khayatnezhad M, Ghadimi N. Model parameters identification of the PEMFCs using an improved design of Crow Search Algorithm. Int J Hydrogen Energy. 2022;47(79):33839–49. doi:10.1016/j.ijhydene.2022.07.251.
2. Mohammedi A, Sahli Y, Ben Moussa H. 3D investigation of the channel cross-section configuration effect on the power delivered by PEMFCs with straight channels. Fuel. 2020;263:116713. doi:10.1016/j.fuel.2019.116713.
3. Rostami L, Mohamad Gholy Nejad P, Vatani A. A numerical investigation of serpentine flow channel with different bend sizes in polymer electrolyte membrane fuel cells. Energy. 2016;97(6):400–10. doi:10.1016/j.energy.2015.10.132.
4. Shen J, Tu Z, Chan SH. Evaluation criterion of different flow field patterns in a proton exchange membrane fuel cell. Energy Convers Manag. 2020;213(13):112841. doi:10.1016/j.enconman.2020.112841.
5. He Z, Zhao W, Jian H, Mao J, Wang Z, Dong W. Performance improvement of solid oxide fuel cell by neural network and multi-objective optimization algorithm. J Renew Sustain Energy. 2025;17(6):064702. doi:10.1063/5.0283265.
6. Spreafico C, Thonemann N. Prospective life cycle assessment of proton exchange membrane fuel cell. Comparing data from patents and papers. Int J Hydrogen Energy. 2025;99(57):45–52. doi:10.1016/j.ijhydene.2024.12.211.
7. Sun F, Su D, Yin Y, Pang B, Guo J. Effects of combined baffles on the proton exchange membrane fuel cell performance. Int J Electrochem Sci. 2022;17(11):221134. doi:10.20964/2022.11.18.

8. Perng SW, Wu HW. Effects of internal flow modification on the cell performance enhancement of a PEM fuel cell. J Power Sources. 2008;175(2):806–16. doi:10.1016/j.jpowsour.2007.09.095.
9. Tan Q, Lei H, Liu Z. Numerical simulation analysis of the performance on the PEMFC with a new flow field designed based on constructal-theory. Int J Hydrogen Energy. 2022;47(23):11975–90. doi:10.1016/j.ijhydene.2022.01.243.
10. Wang C, Zhang Q, Lu J, Shen S, Yan X, Zhu F, et al. Effect of height/width-tapered flow fields on the cell performance of polymer electrolyte membrane fuel cells. Int J Hydrogen Energy. 2017;42(36):23107–17. doi:10.1016/j.ijhydene.2017.07.136.
11. Liu H, Tan J, Cheng L, Yang W. Enhanced water removal performance of a slope turn in the serpentine flow channel for proton exchange membrane fuel cells. Energy Convers Manag. 2018;176(10):227–35. doi:10.1016/j.enconman.2018.08.104.
12. Xu G, Yu Z, Xia L, Wang C, Ji S. Performance improvement of solid oxide fuel cells by combining three-dimensional CFD modeling, artificial neural network and genetic algorithm. Energy Convers Manag. 2022;268:116026. doi:10.1016/j.enconman.2022.116026.
13. Chen Z, Zuo W, Zhou K, Li Q, Huang Y. Multi-objective optimization of proton exchange membrane fuel cells by RSM and NSGA-II. Energy Convers Manag. 2023;277(7867):116691. doi:10.1016/j.enconman.2023.116691.
14. Xia Y, Guo C, Dong E, Chen L, Tao W. Topology optimization of gas channels in proton exchange membrane fuel cells. Int J Heat Mass Transf. 2024;222(4):125147. doi:10.1016/j.ijheatmasstransfer.2023.125147.
15. Velisala V, Pullagura G, Golagani NS. Numerical study of serpentine flow field designs effect on proton exchange membrane fuel cell (PEMFC) performance. Chem Prod Process Model. 2021;16(1):55–66. doi:10.1515/cppm-2020-0023.
16. Wang Y, Wang X, Fan Y, He W, Guan J, Wang X. Numerical investigation of tapered flow field configurations for enhanced polymer electrolyte membrane fuel cell performance. Appl Energy. 2022;306(5):118021. doi:10.1016/j.apenergy.2021.118021.
17. Jian H, He Z, Mao J, Liang F, Wang Z, Fu Y. Comparison and optimization of electrochemical and thermal performances of SOFC with different configurations of a metal foam flow field. J Renew Sustain Energy. 2024;16(5):054702. doi:10.1063/5.0223633.
18. Haghayegh M, Eikani MH, Rowshanzamir S. Modeling and simulation of a proton exchange membrane fuel cell using computational fluid dynamics. Int J Hydrogen Energy. 2017;42(34):21944–54. doi:10.1016/j.ijhydene.2017.07.098.
19. Bielefeld NM, Sørensen RD, Jørgensen M, Kure KS, Berning T. Operating proton exchange membrane fuel cells at a constant relative humidity. ECS Trans. 2022;108(7):3–15. doi:10.1149/10807.0003ecst.
20. He Z, Liang S, Mao J, Zhao W, Zuo M, Fu Y. Thermal management of turbine disc cavity system using FFBPNN and NSGA II algorithm. Case Stud Therm Eng. 2025;68(2):105954. doi:10.1016/j.csite.2025.105954.